Research Article

Correlation of microstructure, mechanical properties, and residual stress of 17-4 PH stainless steel fabricated by laser powder bed fusion

M.S. Moyle [a], N. Haghdadi [a,*], V. Luzin [b,c], F. Salvemini [b], X.Z. Liao [d,e], S.P. Ringer [d,e], S. Primig [a,*]

[a] School of Materials Science & Engineering, UNSW Sydney, NSW 2052, Australia
[b] Australian Nuclear Science and Technology Organisation (ANSTO), NSW 2234, Australia
[c] School of Engineering, The University of Newcastle, NSW 2308, Australia
[d] Australian Centre for Microscopy & Microanalysis, The University of Sydney, NSW 2006, Australia
[e] School of Aerospace, Mechanical and Mechatronic Engineering, The University of Sydney, NSW 2006, Australia

A B S T R A C T

17-4 precipitation hardening (PH) stainless steel is a multi-purpose engineering alloy offering an excellent trade-off between strength, toughness, and corrosion properties. It is commonly employed in additive manufacturing via laser powder bed fusion owing to its good weldability. However, there are remaining gaps in the processing-structure-property relationships for AM 17-4 PH that need to be addressed. For instance, discrepancies in literature regarding the as-built microstructure, subsequent development of the matrix phase upon heat treatment, as well as the as-built residual stress should be addressed to enable reproducible printing of 17-4 builds with superior properties. As such, this work applies a comprehensive characterisation and testing approach to 17-4 PH builds fabricated with different processing parameters, both in the as-built state and after standard heat treatments. Tensile properties in as-built samples both along and normal to the build direction were benchmarked against standard wrought samples in the solution annealed and quenched condition (CA). When testing along the build direction, higher ductility was observed for samples produced with a higher laser power (energy density) due to the promotion of interlayer cohesion and, hence, reduction of interlayer defects. Following the CA heat treatment, the austenite volume fraction increased to ∼35 %, resulting in a lower yield stress and greater work hardening capacity than the as-built specimens due to the transformation induced plasticity effect. Neutron diffraction revealed a slight reduction in the magnitude of residual stress with laser power. A concentric scanning strategy led to a higher magnitude of residual stress than a bidirectional raster pattern.

© 2024 Published by Elsevier Ltd on behalf of The editorial office of Journal of Materials Science & Technology.
This is an open access article under the CC BY license (http://creativecommons.org/licenses/by/4.0/)

1. Introduction

The continued development of additive manufacturing (AM) for metals has been of great interest to many engineering industries. AM allows engineers to break free from design constraints imposed by traditional manufacturing methods as parts can be produced with highly intricate and specialised designs well-suited to achieve superior performance [1,2]. 17-4 precipitate hardening (PH) stainless steel has been identified as the alloy which experienced the biggest growth in AM profitability in 2021 [3]. The high strength and toughness combined with high corrosion resistance of 17-4 PH make it suitable for numerous applications, including in the aerospace, marine, and petrochemical industries. Under conventional processing routes, it is a martensitic stainless steel which undergoes precipitation hardening by the formation of Cu rich precipitates on the nanoscale during ageing heat treatments [4,5]. After casting, a typical thermal processing route for 17-4 PH is to hold at 1040 °C for 1 h followed by a water quench, creating a martensitic matrix supersaturated with Cu [5,6]. This heat treatment state is referred to as CA (condition A). A subsequent ageing treatment of 1 h at 480 °C (the H900 ageing treatment) has been empirically found to give the greatest strengthening effect [5,7].

Although 17-4 PH stainless steel is now widely used in metal AM, existing literature makes contrasting observations relating to its structure and properties [8]. Whilst some studies into the as-printed material report predominantly martensitic microstructures [9–11] others report predominantly austenite [9,12] or δ-ferrite microstructures [11,13-16]. Some researchers have found that heat treating to CA can form a fully martensitic matrix in laser

powder bed fusion (LPBF) 17-4 PH, resulting in the anticipated effects of conventional thermal processing [17,18], whilst others have found that even the CA heat treatment does not guarantee a fully martensitic matrix [19,20] resulting in knock on effects on the ageing response [10,20,21]. Some have attributed these differences in phase behaviour to compositional differences in the material, likely due to different powder feedstocks and fabrication atmospheres [20,22,23]. These differences would result in a different Cr_{eq}/Ni_{eq} ratio, a compositional term assessing the relative stability of austenite vs ferrite or martensite in the matrix of a steel [24]. Changes in phase behaviour can have significant effects on the mechanical properties of 17-4 PH, such as strength and toughness. This is why coupling the processing parameters to the microstructure and properties remains challenging.

Further, the LPBF process can result in significant residual stresses in builds. This is due to cyclic, rapid, and localised cooling and reheating of the material layer by layer [25,26]. A consequential residual stress is also incurred on the build plate. Upon removal of the part from the build-plate, non-uniform stress relaxation causes residual stresses to redistribute in the final part. Unless a form of heat treatment is applied, these resultant residual stresses will remain in the printed component and can impact service performance. This can be advantageous, with residual compressive stress states resisting the opening of cracks leading to greater fatigue performance [27]. However, large, and unfavourably aligned residual stresses can lead to poor mechanical properties. Poorly chosen process parameters and build geometries can result in large part distortion, cracking, and delamination during printing, resulting in an overall reduction in print quality to the detriment of part strength and ductility [25,28–30]. AM-induced intragranular residual stresses can negatively affect the part yield strength due to resultant back stresses [31].

Some investigations into the residual stress in LPBF parts have been undertaken using several techniques which measure the amount of stress relaxation after building, such as hole-drilling and build deflection measurement [25,27,32], however the data from such techniques is qualitative and has low spatial resolution. Diffraction techniques, using either X-rays or neutron beams, can directly measure lattice strains via the shift in the Bragg angle to non-destructively evaluate residual stress [32]. Compared to X-ray diffraction, neutron diffraction has a greater penetration depth (a few centimeters) so residual stresses can be measured through the thickness of larger AM builds [27]. Another advantage of neutron diffraction is that triaxial residual stress results can be obtained by taking measurements along multiple axes. A number of previous studies have investigated the residual stress distribution in LPBF builds using neutron diffraction [33–37], finding that residual stress can be reduced by remelting and reducing the scan island size. So far, no studies using neutron diffraction have investigated the effect of a uniform concentric scanning strategy, as considered in this study. Such patterns are of great interest given the unusual and inhomogeneous phase behaviour that they can produce in as-built samples [14], but advantageous applications may only be realised with a more thorough understanding of the residual stresses they incur.

The current work aims to address the gaps in knowledge around mechanical properties of LPBF 17-4 PH stainless steel builds and link this to the as-built microstructure and residual stress distributions incurred by the fabrication process. It aims to elaborate on the effect of laser power and scanning strategy on the residual stress. The atypical post heat-treatment microstructures and their mechanical behaviours are evaluated. By coupling properties with processing parameters, the results of this work will inform future engineers on the achievable microstructures and mechanical properties of LPBF 17-4 PH as well as the residual stress distributions and magnitudes formed in LPBF builds.

2. Materials and methods

17-4 PH stainless steel powder was provided by 3D systems. Lashgari et al. [38] analysed the same powder using laser diffraction, reporting that the D_V10 (i.e., particle diameter larger than exactly 10 % of measured particles), D_V50, and D_V90 values for this powder were 4.38, 11.8, and 29.4 µm, respectively. Samples were printed in an N_2 gas atmosphere using a 3D Systems ProX 300 LPBF machine using a laser spot size of 90 µm. No preheating was applied to the build plate. The various processing parameters utilised in this study are summarised in Table 1. Hatch spacing, scanning speed, and layer height were selected from manufacturer recommended values and kept constant between printing conditions. The hexagonal scanning strategy consists of a bidirectional raster scan rotated 90° between each layer comprising of hexagonal island scans measuring 50 mm between opposite vertices. The raster scan was the same as the hexagonal scanning strategy without any island pattern within the scan. The concentric scanning strategy used a bidirectional scan tracing the outer-most edge of each layer first, then moving progressively inwards to fully melt each layer. In the case of the hexagonal and raster scans, the bidirectional scan was rotated 90° on and off every layer of the build. The directions of these scans were 60° offset from the principal axes of the build dimensions. Schematic diagrams of these printing strategies are provided in Fig. 1. Specimens were printed as cubes of 10 mm × 10 mm × 10 mm for neutron diffraction and tomography analysis. Specimens were also printed as dog-bones for tensile testing. These samples had a gauge length of 27.29 mm with a cross section of 6.25 mm × 2 mm (in accordance with ASTM E8-22 standard subsize dimensions). Some dog-bone samples were fabricated with the loading direction perpendicular to the build direction (BD), hereafter termed "horizontally built", and others were fabricated with the loading direction parallel to BD, hereafter termed "vertically built" samples, in order to investigate the effect of build orientation on the tensile properties. Samples for Charpy impact testing were fabricated with a geometry of 5 mm × 10 mm × 55 mm with the 55 mm dimension parallel to the build direction. A standard V-notch was machined into the mid-point on one of the 5 mm × 55 mm faces (in accordance with ASTM E23-07a).

After fabrication, samples were mechanically tested in three different post-built heat treatment conditions: The as-built condition (AB), after a solution annealing treatment at 1040 °C for 1 h followed by a water quench (CA), and after heat treating to CA followed by an ageing treatment at 480 °C for 1 h followed by air cooling (CA-H900). Heat treatments were performed in air using a Nabertherm LHTCT 03/16/C550 high temperature furnace.

Table 1
LPBF processing parameters for the samples considered in this study. Note: HP = High power, LP = Low power.

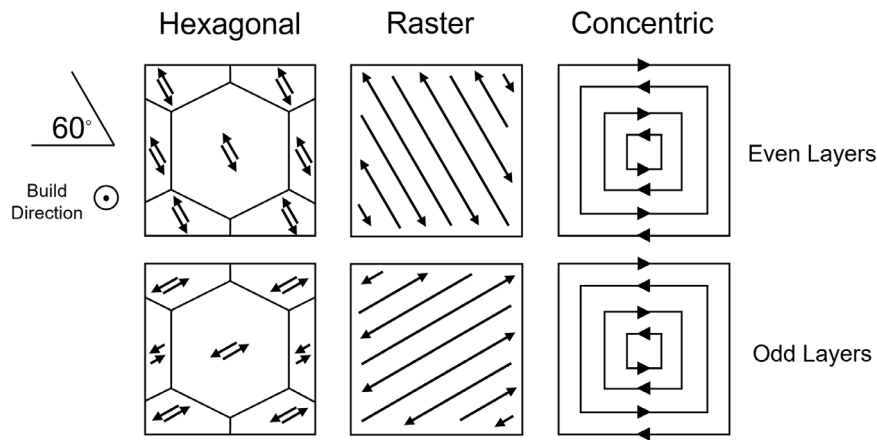| Condition name	Laser power (W)	Scanning speed (mm s⁻¹)	Hatch spacing (µm)	Layer height (µm)	Scanning pattern
Hex LP	127.5	1200	50	40	Hexagonal
Hex HP	161.5	1200	50	40	Hexagonal
Raster	127.5	1200	50	40	Raster
Concentric	127.5	1200	50	40	Concentric

Fig. 1. Schematic diagrams of the scanning strategies used in this research.

Table 2
Composition (wt%) of the 17-4 PH powder and an LPBF build.

	Fe	C	Mn	Si	S	P	Ni	Cr	Mo	Cu	V	Nb	Ti	Al	N
Powder	73.49	0.03	0.87	0.71	<0.01	0.03	4.34	16.1	0.13	3.81	0.04	0.32	0.02	0.01	0.10
LPBF build	72.19	0.02	0.90	0.92	<0.01	0.03	4.57	16.8	0.12	3.92	0.06	0.37	<0.01	0.01	0.09
Error (±)	Bal	0.005	0.05	0.04	0.005	0.005	0.1	0.2	0.05	0.1	0.007	0.02	0.005	0.005	0.02

X-Ray Diffraction analysis (XRD) was performed on planes sectioned along the build direction using an Empyrean PANalytical Powder X-ray diffractometer in order to measure the volume fractions of each phase in the builds via Rietveld refinement. Measurements were taken midway along the build height, away from any build surfaces.

Atom Probe Tomography (APT) was performed using a CAMECA LEAP 3000 Si which had a detector efficiency of 55 %. Datasets were collected from regions midway along the build height, away from any build surfaces. During dataset collection, a temperature of 50 K, a pulse rate of 200 kHz, and a pulse fraction of 20 % were used. Datasets were reconstructed based on crystallographic information. The APT datasets were reconstructed via CAMECA's Integrated Visualization & Analysis Software (IVAS) and AP suite 6.0.

Composition analysis was done for both a sample of the powder and a section of a build using inductively coupled plasma atomic emission spectroscopy (ICP-AES) at a commercial laboratory. These compositions are provided in Table 2.

Tensile tests were conducted at room temperature using an Instron 5982 tensile testing machine and an MTS laser extensometer Lx500. The strain rate during testing was 1 mm min^{-1}. At least two samples were tested for each condition.

The fracture surfaces and as-received powder were investigated with a JEOL 7001f scanning electron microscope using secondary electron imaging. Electron backscattered diffraction (EBSD) analyses of polished cross-sections immediately below the fracture surface were performed on a JEOL 7001f using an accelerating voltage of 20 kV, a probe current of 13 nA, a 6 × 6 binning, and a Hikari-EDAX camera. Data analysis was done using TSL OIM 8.0 software. The samples were prepared by grinding to 4000 grit with SiC paper, and polishing with 3 μm and 1 μm diamond suspensions successively. The final polishing step either used 0.04 μm OPU colloidal silica, for tested tensile specimens, or electropolished at 25 V for 30 s using Struers A2 electrolyte, for pre-testing microstructure analysis. Comparative analysis showed that no discernible phase transformation was induced by the use of OPU polishing on the tested tensile specimens. Energy dispersive spectroscopy (EDS) was used to evaluate compositional differences across the fracture surfaces.

Selected samples were also examined by transmission Kikuchi diffraction (TKD) which provides higher resolution maps than standard EBSD [39]. Thin foil preparation for transmission Kikuchi diffraction (TKD) was performed using standard twin jet electropolishing [40] with a Struers A2 electrolyte. TKD was carried out in a ThermoFisher Helios G4 Xe PFIB using 30 kV accelerating voltage, 6.4 nA probe current, 4 mm working distance, −10° stage tilt, an Oxford Instruments Aztec Symmetry system, sensitivity preset, and a 25 nm step size.

Residual stress measurements were performed using the KOWARI strain scanner at Australia's Nuclear Science and Technology Organisation (ANSTO) [41] on cubic specimens. For the three-dimensional (3D) residual stress analysis on cubic builds, wavelengths of 1.67 Å and 1.53 Å were used to observe the shift of the diffraction peak (*d*-spacing) from the (211) planes in body-centred cubic (BCC) ferrite and the (311) planes in face centred cubic (FCC) austenite respectively. The nominal gauge volume for each measurement in these samples was 1.3 mm × 1.3 mm × 1.3 mm. Measurements were taken at a scattering angle of 90°.

Since two matrix phases, BCC and FCC, are present within the microstructure, the stress analysis treats the material as a composite with analysis of phase strains and stresses with separation of the macro-stress and micro-stress [42]. The true d_0 (stress-free *d*-spacing) could not be obtained without, for example, the dissolution of one phase and removal of any remaining stresses. Consequently, an assumption of the constant d_0 for both phases was used for the evaluation of the phase strains. This was based on the boundary conditions, i.e., residual stress must be 0 at a free surface in the normal direction, and a force condition, that the integral of normal residual stresses of a full cross section must be 0. Using such "reference" d_0 values, the macro-stress can be evaluated provided that phase volume fractions are known. However, the hydrostatic micro-stresses that are most likely present due to mismatch of the elastic, plastic, and thermal properties of BCC and FCC phase remain unknown and are therefore not discussed. The reliably reconstructed macro-stress is further referred to simply as "stress".

Neutron computed tomography was conducted on the imaging beamline DINGO at ANSTO [43]. The investigation was con-

ducted in high resolution acquisition mode (length to diameter ratios of up to 1000). The ANDOR MARANA sCMOS detector was configured to yield images with a pixel size of 17 μm by setting a 70 mm × 50 mm field of view with a 100 mm lens coupled with a gadolinium oxysulphide scintillation screen with a thickness of 30 μm. Projections were acquired with an equiangular step of 0.17° over 360° and an exposure time of 90 s. Flat field normalization with dose correction and dark current subtraction were applied to each dataset. The data was processed using the NeuTomPy toolbox [44]. The obtained slices were recomposed and evaluated using Avizo 9.1 software.

3. Results

3.1. As-Built and heat-treated microstructures

The results of XRD phase fraction analysis can be viewed in Table 3. It shows that, contrary to the typical behaviour of this alloy following this thermal history [4,15,19], the FCC phase fraction increases after the CA heat treatment. Typically, applying the CA heat treatment to 17-4 PH results in a uniform microstructure of close to 100 % martensite (BCC).

Table 3
Phase volume fractions (V_f) resultant from different printing and heat treatment conditions as determined by X-Ray diffraction analysis.

	BCC V_f (%)	FCC V_f (%)
Hex LP – As-built	96.1 ± 1.7	3.9 ± 1.2
Hex HP – As-built	95.8 ± 3.8	4.2 ± 2.9
Hex LP – CA	63.0 ± 3.4	37.0 ± 4.5
Hex HP – CA	68.2 ± 5.1	31.8 ± 9.3

Fig. 2 shows EBSD data collected from the bulk regions of samples which did not undergo mechanical testing. Comparing the inverse pole figure (IPF) maps in Fig. 2(a) and (d), it is easily seen that the average BCC grain size in the as-built state increases significantly with increasing laser power. The average as-built grain BCC grain area was 94 ± 8, 249 ± 12, and 114 ± 9 μm² for the Hex LP, Hex HP, and Raster samples, respectively. The phase maps presented in Fig. 2(b) and (e) are consistent with the XRD results shown in Table 3, demonstrating that the increase in laser power between Hex LP and Hex HP did not lead to a significant change in the phase volume fractions. Fig. 2(g–l) demonstrate the extent of grain refinement and increase in austenite volume fraction as a result of the CA heat treatment. Comparing the pole figures pre-
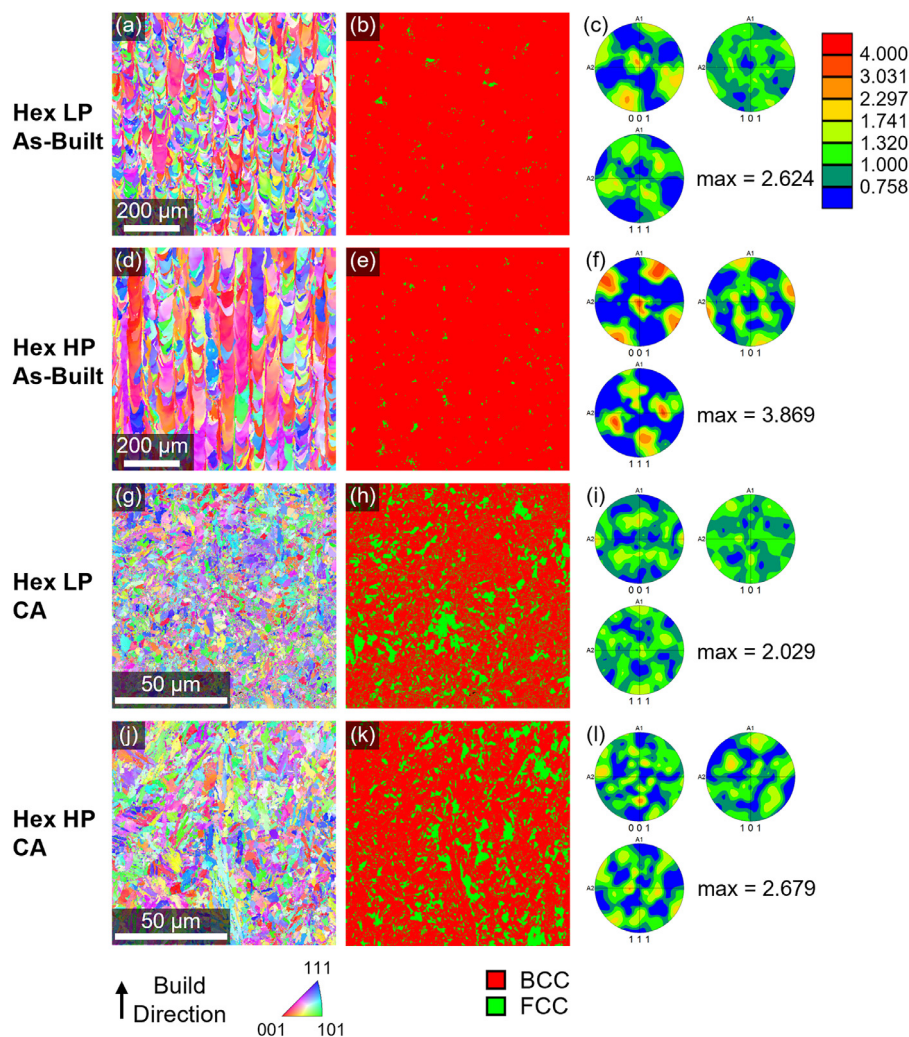

Fig. 2. EBSD Analysis of samples before mechanical testing (a–c) Hex LP As-Built, (d–f) Hex HP As-Built, (g–i) Hex LP CA, (j–l) Hex HP CA. (a, d, g, j) IPF Maps, (b, e, h, k) Phase Maps, (c, f, i, l) Pole figures showing BCC texture along BD. Note that each of these pole figures uses the same colour scale. Colour in the IPF maps shows orientation along the BD in each case. Area-weighted average BCC grain areas were evaluated for each EBSD map to be 94 ± 8 μm² (Hex LP As-built), 249 ± 12 μm² (Hex HP As-built), 1.79 ± 0.05 μm² (Hex LP CA), 2.56 ± 0.11 μm (Hex HP CA). Note: the difference in length scale between different IPF and phase maps.
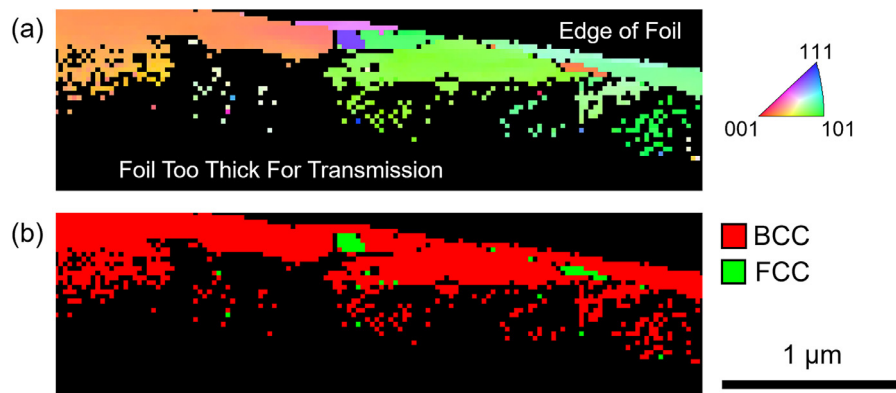
Fig. 3. Representative TKD map of the Hex LP CA build (a) IPF map, (b) Phase map clearly indicating the presence of nanoscale FCC regions along grain boundaries.

sented for each of the sample conditions (Fig. 2(c, f, i)), it can be seen that the BCC phase's clear cube texture in the as-built specimens is eliminated by the CA heat treatment. Comparing the results for the Hex LP CA and Hex HP CA samples in Fig. 2, no significant differences in the microstructure are apparent.

The fine scale of the multi-phase microstructure of the samples following the CA heat treated samples exceeds the resolution of the EBSD analysis in Fig. 2. For this reason, TKD was performed to characterise the nanoscale FCC phase. These results are presented in Fig. 3, showing that nanoscale FCC grains are present at grain boundaries of larger BCC grains.

Fig. 4 shows the distribution of Cu atoms within CA and CA-H900 samples from APT data. In both heat treatment conditions, no Cu clustering/precipitation behaviour is visible in the sections of the atom maps (Fig. 4(a, b)). The Cu first nearest neighbour distributions for these samples plotted in black in Fig. 4(c) and (d), do not show any significant deviations from the comparable randomised nearest neighbour distributions.
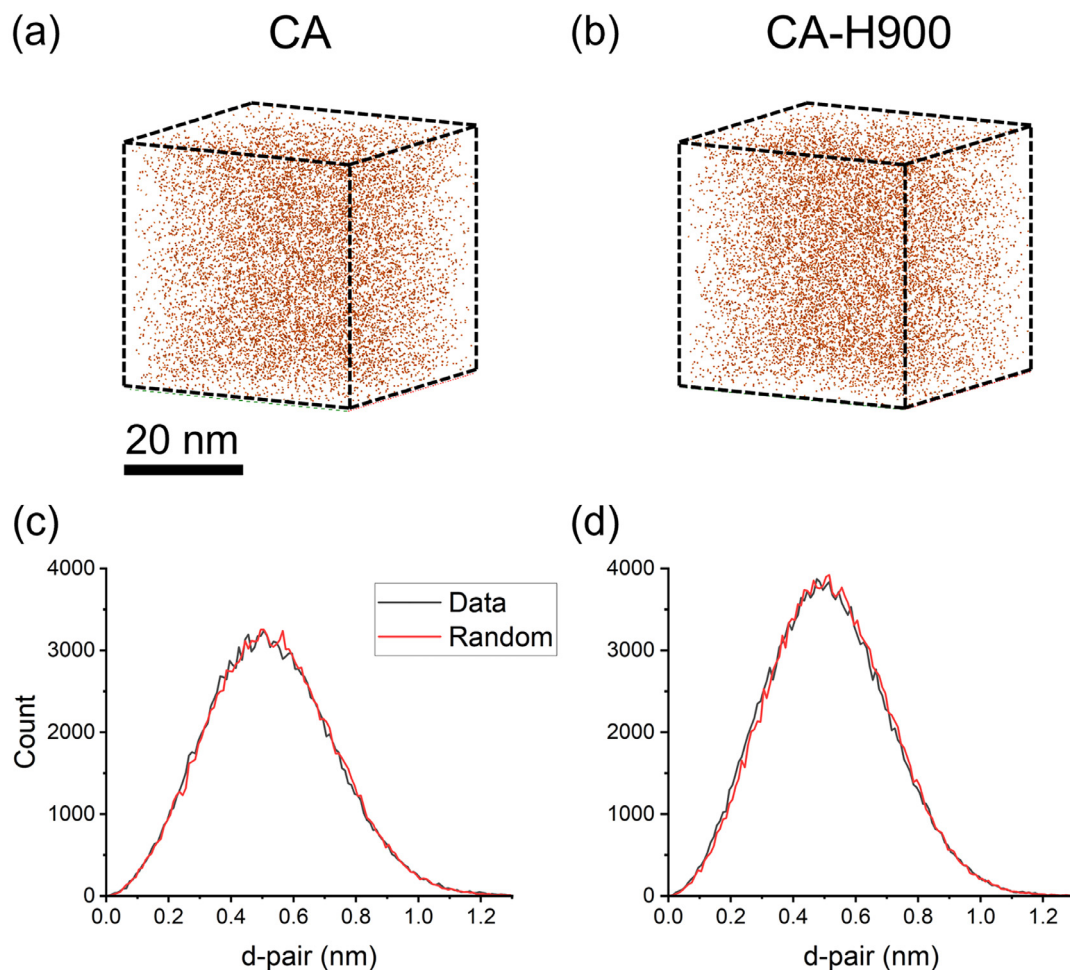

Fig. 4. Atom probe data showing Cu distributions in the (a, c) CA, (b, d) CA-H900 conditions. (a, b) Cu atom maps from 20 nm × 20 nm × 20 nm cubic sections of APT datasets. (c, d) Nearest neighbour distributions for Cu within the entire APT datasets.

Table 4

Summary of mechanical properties from tensile tests of all horizontally printed and vertically printed 17-4 PH samples. Standard ASM wrought 17-4 PH mechanical properties are also shown. Where anomalous yield behaviour has occurred, the lower yield stress is shown.

	Yield Stress (MPa)	UTS (MPa)	Elongation to failure
Standard wrought [6]			
CA-H900	1055	1380	0.150
Vertically built			
Hex LP – AB	795 ± 20	892 ± 15	0.057 ± 0.020
Hex HP – AB	763 ± 45	931 ± 6	0.187 ± 0.010
Raster – AB	854 ± 17	947 ± 1	0.105 ± 0.020
Horizontally built			
Hex LP – AB	878	986	0.134
Hex HP – AB	822 ± 30	963 ± 20	0.147 ± 0.020
Raster – AB	888 ± 40	996 ± 20	0.159 ± 0.003
Hex LP – CA	281 ± 2	941 ± 6	0.156 ± 0.007
Hex HP – CA	338 ± 10	943 ± 30	0.118 ± 0.020
Raster – CA	286 ± 2	951 ± 2	0.161 ± 0.001
Hex LP – CA-H900	All Anomalous		
Hex HP – CA-H900	349 ± 20	937 ± 30	0.141 ± 0.001
Raster – CA-H900	338 ± 3	923 ± 20	0.169 ± 0.020

3.2. Mechanical testing

The tensile properties of the samples can be viewed in Table 4, with representative engineering stress vs strain curves displayed in Fig. 5. Comparing the mechanical properties for samples tested in the as-built state, for each combination of processing parameters, samples printed vertically have both lower average yield strengths

and ultimate tensile strengths than those printed horizontally. It can also be seen that vertically built Hex HP samples have a significantly greater elongation to failure than those printed with either Hex LP or Raster samples. For horizontally built samples, the average elongation to failure is comparable between all printing parameters, but Hex HP samples showed slightly decreased average yield and ultimate tensile strengths compared to Hex LP or Raster samples. In comparison to standard wrought samples in the CA-H900 condition [6], the as-built properties presented here show reduced yield and ultimate tensile stresses, with some showing comparable elongation to failure.

Table 4 shows that the greatest yield stresses and ultimate tensile strengths (UTS) in LPBF fabricated parts occurred within samples in the as-printed state. After heat treating to CA, the yield stress significantly decreased while the work hardening capacity of the material increased. This resulted in a slight decrease in UTS for all printing conditions. Many samples in CA exhibited a yield plateau in the stress strain curve. Additionally, many of the stress strain curves for the heat-treated samples show secondary discontinuities, as indicated by yellow arrows in Fig. 5. Furthermore, ageing to the H900 condition after the CA heat treatment did not result in any appreciable difference in mechanical properties.

The results of Charpy impact testing show no great variation in impact toughness with changing processing parameters between Hex LP (1.4 ± 0.1 MJ m^{-2}), Hex HP (1.4 ± 0.1 MJ m^{-2}), and Raster (1.6 ± 0.1 MJ m^{-2}). Wrought 17-4 PH exhibits a Charpy impact toughness of 2.710 MJ m^{-2} and 0.813 MJ m^{-2} in the CA and CA-H900 conditions respectively [45].
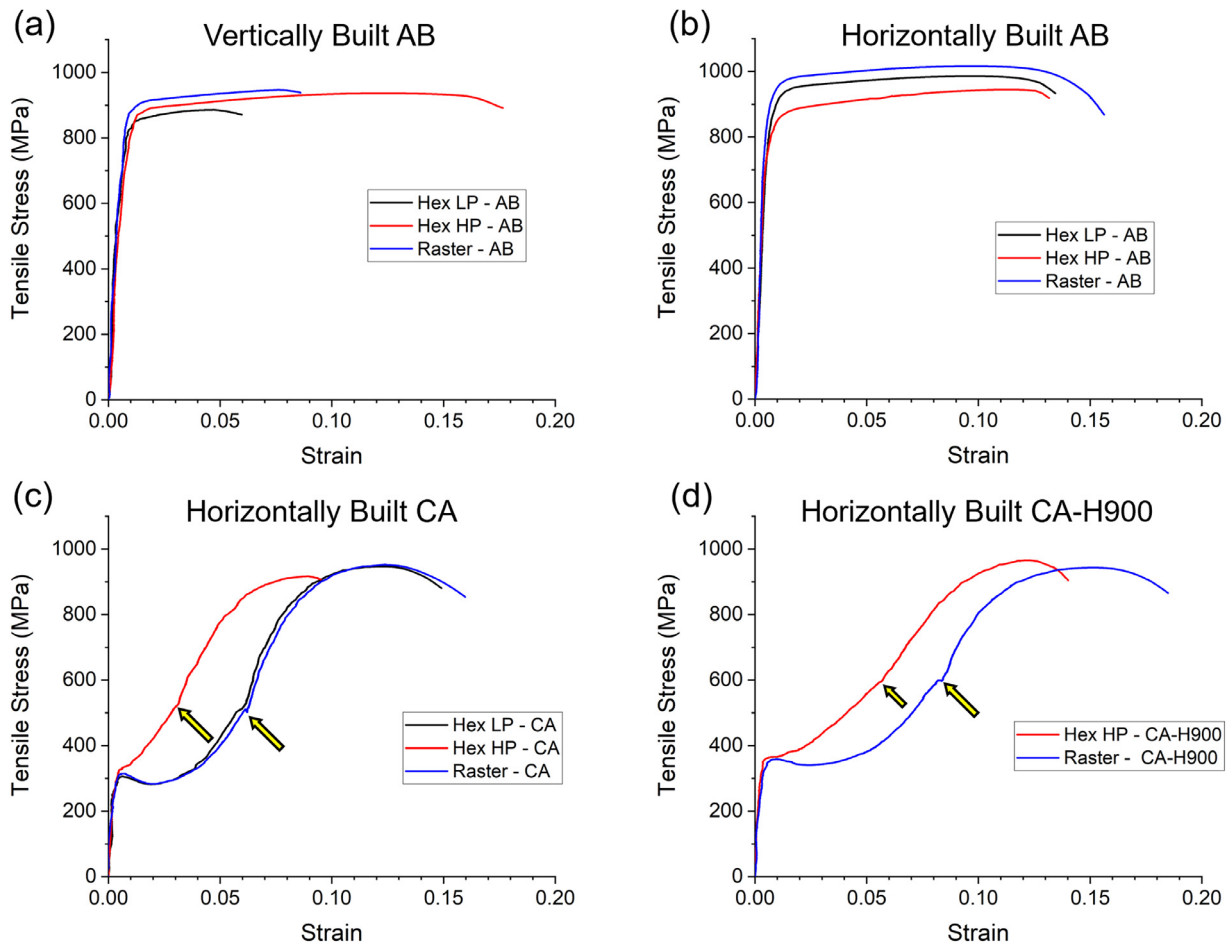

Fig. 5. Representative stress vs strain curves from the tensile tests of LPBF 17-4 PH samples. (a) Vertically Built AB, (b) Horizontally Built AB, (c) Horizontally Built CA, (d) Horizontally Built CA-H900. Yellow arrows indicate secondary discontinuities in the curves.
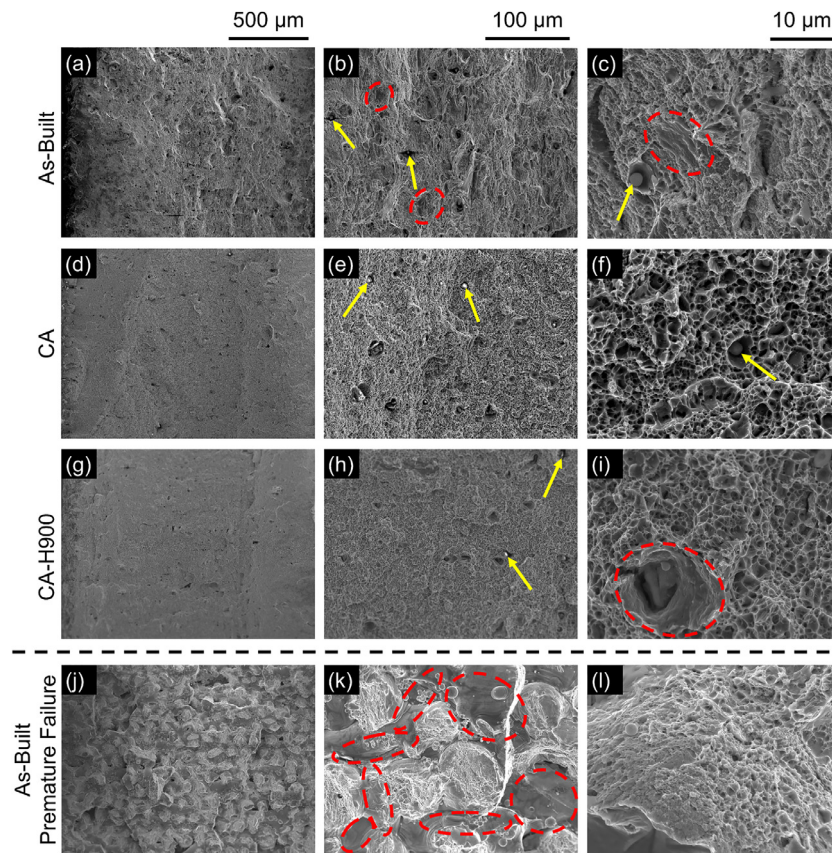
Fig. 6. Representative fracture surfaces from horizontally built tensile test specimens with the (a–i) Raster samples. (a–c) As-built, (d–f) CA, (g–i) CA-H900. (j–l) As-built samples fabricated using Hex LP processing parameters that underwent premature failure. Each scale bar applies to each column of subfigures. Yellow arrows indicate hard particles observed on the surfaces. The red, dashed ellipses indicate smooth regions of the fracture surface.

Fig. 6(a–i) shows representative fracture surfaces for horizontally built Raster tensile specimens in each heat treatment condition at multiple magnification levels. Several differences can be observed comparing these subfigures. In the as-built condition, cracks and ridges can be observed on the fracture surfaces at low magnification. At high magnification, a mixture of dimpled and smoother regions of fracture surface topography can be observed. Smoother crack regions, indicated by the red dashed ellipses, are likely due to the opening of pre-existing lack of fusion pores in the build during failure. Comparing Fig. 6(a) and (d), it can be seen that, after the CA heat treatment, the fracture surface becomes more topographically flat on the 100 s μm length scale. Greater magnifications reveal that the CA and CA-H900 heat treatments also resulted in a fracture surface much more devoid of cracks, showing an almost exclusively dimpled morphology. Fig. 6 shows that all samples following all processing routes contain hard particle inclusions, as indicated by yellow arrows. Energy dispersive spectroscopy (EDS) was undertaken to reveal the composition of these inclusions. The EDS results, presented in Fig. 7, show these particles to be depleted in Fe and rich in Mn and Si both in the as-built and CA states. The inclusion analysed on the fracture surface of the as-built specimen was also enriched in O. These MnSi and MnSiO enriched inclusions were likely incorporated into the builds from impurities in the powder during fabrication. Ageing did not result in any significant differences to the fracture surfaces as compared to the CA state. Fig. 6(j–l) shows the fracture surface of a sample which failed prematurely. This early failure was clearly the result of poor consolidation of the material during printing. Fig. 6(j) shows the fracture surface to contain a large, interconnected network of lack of fusion pores.

Fig. 8 shows representative fracture surfaces from the as-built vertically fabricated samples. Similar to Fig. 6, Fig. 8 also shows that the presence of 90° intersecting smooth defects, highlighted with dashed red ellipses, are abundantly present on the fracture surfaces for the Hex LP samples but are absent for Hex HP samples.

Fig. 9 shows EBSD analyses of the *x-y* plane (as defined in Figs. S1 and S2 in the supplementary material) in the sub surface fracture regions of the horizontally built tensile specimens. These results were taken from the same samples presented in the fracture surfaces in Fig. 6. The pole figures displayed in Fig. 9(a, e, i) show strong ⟨110⟩ textures along the loading direction, as is expected after the plastic deformation of BCC crystals resulting in strain accumulation [46]. For the as-built sample, this is in the form of a ⟨100⟩ cubic texture with ⟨110⟩ along the loading direction whilst the heat-treated samples show ⟨110⟩ fibre textures along the loading direction. However, this is not the case for the prematurely failed sample, shown in Fig. 9(m), which retains its pre-testing ⟨100⟩ cubic texture parallel to BD (Fig. 2). This cube texture is not retained beyond the CA heat treatment. The inverse pole figures clearly show grain refinement between Fig. 9(b, f, j) resulting from the CA heat treatment. Fig. 9(b–d) highlights that regions between scan tracks are prone to porosity. Based on their irregular morphology and periodic alignment, it can be surmised that these pores are the result of lack of fusion between scan tracks. The presence of this level of porosity within the sample, however, did not lead to a significant reduction in strength (yield stress = 927 MPa, UTS = 1016 MPa). After the CA heat treatment, the microstructure experiences significant refinement during which these periodic scan-track grain structures are eliminated, as can be seen comparing Fig. 9(b) with Fig. 9(f) and (j).
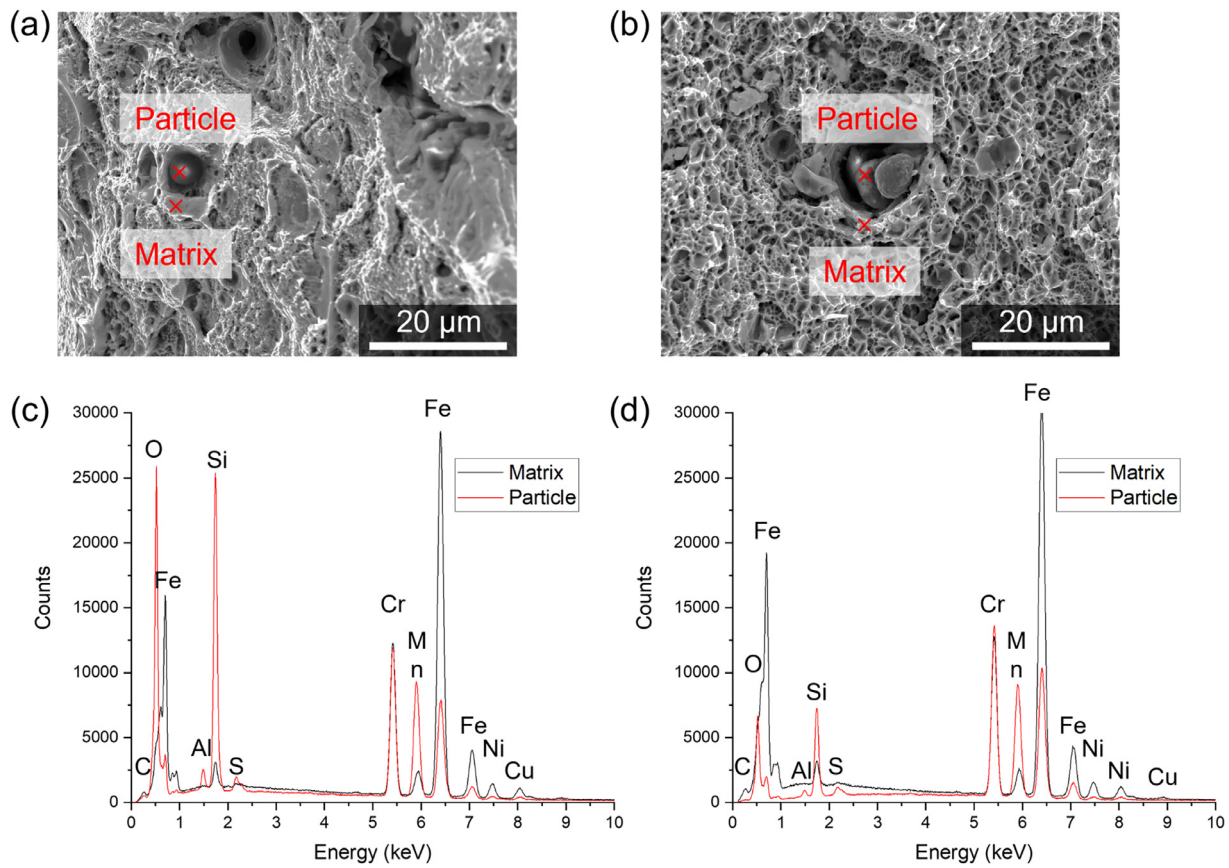
Fig. 7. Energy dispersive X-ray spectroscopy results for particles observed on the tensile fracture surfaces of horizontally built samples printed in condition (3). Micrographs of the (a) as-built, (b) CA fracture surfaces. EDS point scan spectra observed for the (c) as-built, (d) CA surfaces. Red crosses indicate where the point scans were taken in each case.
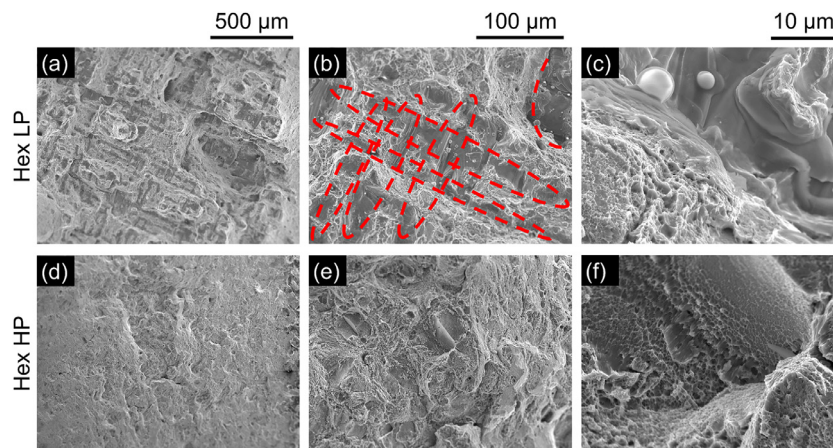

Fig. 8. Representative fracture surfaces from as-built vertically built tensile tests. (a–c) Hex LP (d–f) Hex HP. Red, dashed ellipses indicate smooth regions of the fracture surface.

Due to the differing scale of the as-built grain structure to the CA and CA-H900 grain structures, many of the features in the heat-treated microstructures are not well resolved in Fig. 9. As such, Fig. 10 shows higher magnification EBSD scans from the same regions as Fig. 9. In Fig. 10(a), many grains rotate towards ⟨110⟩ along the loading direction, as highlighted by the increase of datapoints in green leading up to the fracture surface. This highlights the effect of deformation on grain orientation. Comparing the IPF maps shown in Fig. 10(a, e, i), not only is grain refinement by the CA heat treatment highlighted, but the presence of a martensitic grain structure, composed of packets and laths, rather than a ferritic grain structure is also apparent. The Kernel Average Misorientation

(KAM) maps presented in Fig. 10 show an increase in the average misorientation within grains at the fracture surface of the CA-H900 samples as compared to the CA sample.

The reduction in the austenite volume fraction resultant from mechanical testing can be clearly observed when comparing the phase distribution maps in Figs. 9 and 10 to the phase distribution map in Fig. 2(c).

3.3. Residual stress analysis

Fig. 11 shows the 3D residual stress distribution within three cubic builds: Hex LP, Hex HP, and Concentric. The grid of mea-
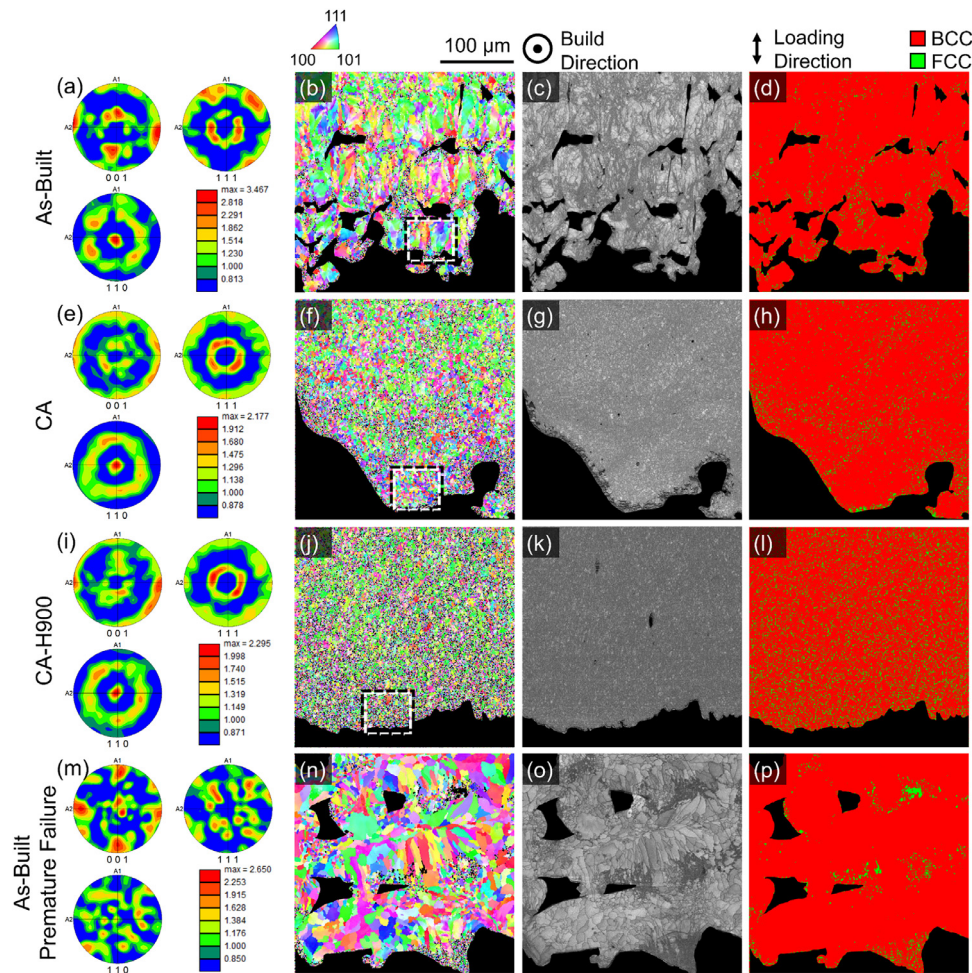
Fig. 9. Results from EBSD at sub-fracture surface regions of horizontally built tensile specimens. (a–d) As-built, (e–h) CA, (i–l) CA-H900, (m–p) An as-built sample which failed prematurely. (a, e, i) Pole figures showing BCC texture. The centre of each pole figure shows the loading direction. (b, f, j) Inverse pole figure maps for the BCC phase with colour showing grain orientation along the loading direction. (c, g, k) Image quality maps. (d, h, l) Phase maps. The data presented in (a–l) relates to Raster samples and (m–p) a Hex LP sample which failed prematurely. Note: The fracture surface is located at the bottom of these maps, at the transition to the black regions.

Table 5
Maximum and minimum residual stress measurements along each axis for each build. Stress values are given in MPa.

	σ_{zz} Max	σ_{zz} Min	σ_{xx} Max	σ_{xx} Min	σ_{yy} Max	σ_{yy} Min
Hex LP	256 ± 17	−315 ± 17	270 ± 17	−264 ± 17	259 ± 17	−273 ± 17
Hex HP	155 ± 22	−360 ± 22	224 ± 21	−330 ± 21	216 ± 21	−334 ± 21
Concentric	199 ± 14	−1177 ± 14	85 ± 14	−871 ± 14	423 ± 14	−897 ± 14

sured points is shown in black in each case. The heat maps were produced by extrapolation and interpolation of the measured data points. All samples show tensile residual stresses near the surfaces, and compressive residual stresses at their interiors. Similar residual stress profiles as well as stress magnitudes can be observed when comparing the stress distributions in the Hex LP and Hex HP samples. The Concentric sample shows a much higher residual stress magnitude in both tensile and compressive regions than either the Hex LP or Hex HP samples. The distribution of the residual stresses within the Concentric sample is significantly different to the other samples, with an almost cylindrical column of triaxial compressive residual stress orientated along BD at the centre of the build. The residual stresses within this sample, both tensile and compressive, have a significantly greater magnitude than within samples fabricated with the hexagonal scanning strategy.

Table 5 shows the maximum and minimum residual stresses from the measured data points shown in Fig. 11. Comparing the data for the Hex LP and Hex HP cubes shows that printing with a greater laser power resulted in lower maximum tensile stresses along all axes but increases the severity of the maximum compressive residual stresses in the interior. Table 5 also highlights the high triaxial compressive stress in the column at the centre of the Concentric sample.

3.4. Neutron computed tomography

The results of the computed tomography analysis are shown in Fig. 12. Due to the resolution of this technique (pixel size of 17 μm), smaller inclusions and pores are not resolved. The inclusions detected in the Hex LP and Hex HP samples were resolved by their greater attenuation coefficient than that of the embedding matrix. The attenuation coefficient of these inclusions was found to be ∼ 1 cm^{-1}. This allows the inclusions to be related to the presence of manganese as its theoretical attenuation co-
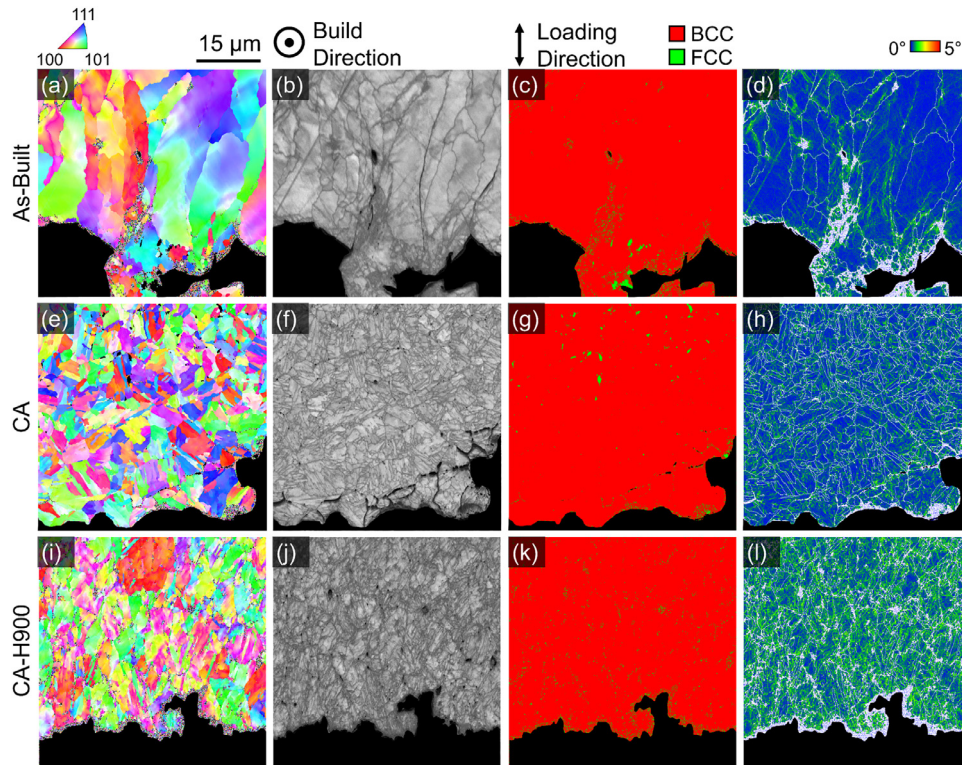
Fig. 10. Results from EBSD at sub-fracture surface regions of horizontally built tensile specimens in the subsections indicated within the subfigures of Fig. 9 (b, f, j). (a–d) As-built, (e–h) CA, (i–l) CA-H900. (a, e, i) Inverse pole figures for the BCC phase with colour showing grain orientation along the loading direction. (b, f, j) Image quality maps. (c, g, k) Phase maps. (d, h, l) Kernel Average Misorientation maps. Note: The fracture surface is located at the bottom of these maps, at the transition to the black regions.
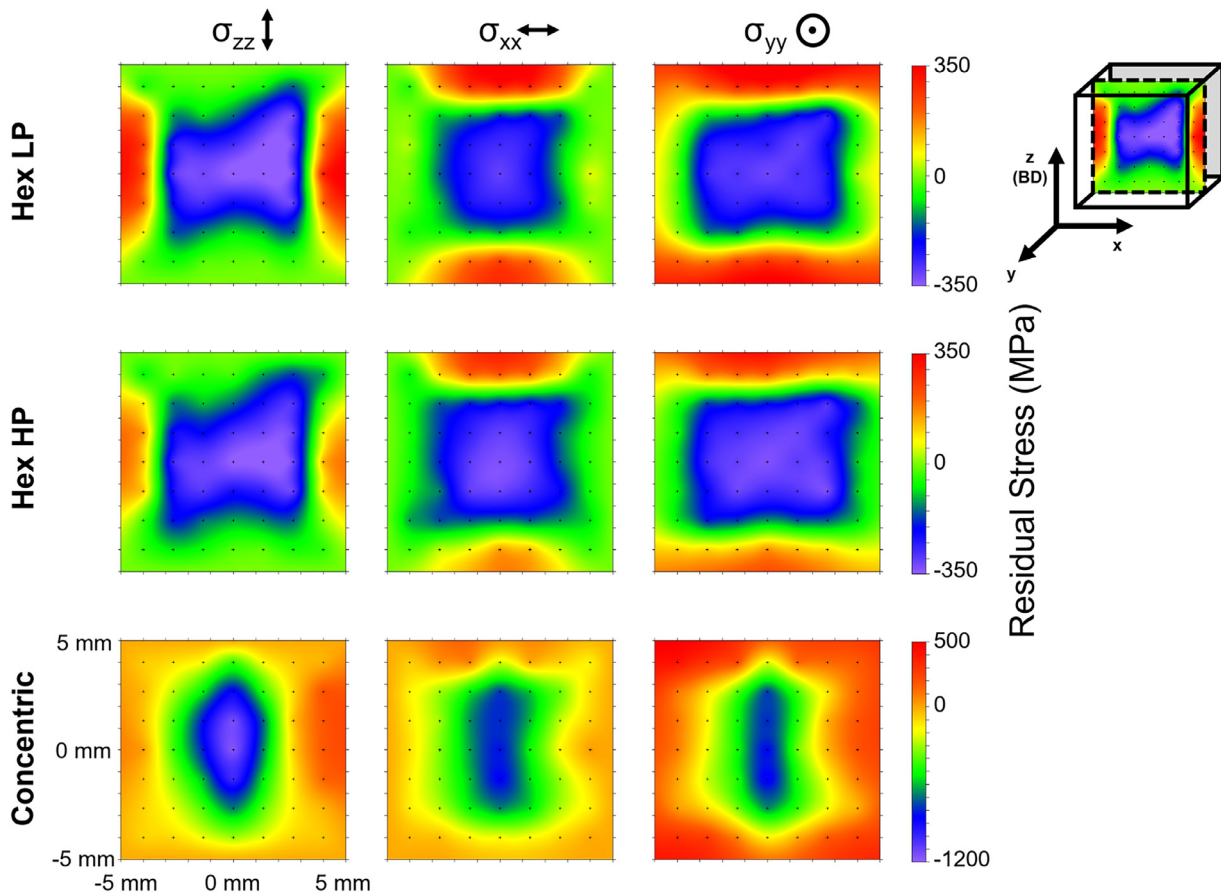

Fig. 11. Residual stress distributions within three 17-4 PH samples fabricated using different LPBF processing parameters. Small black "+" symbols within each subfigure indicate the locations where each neutron diffraction measurement was taken. Top right shows a schematic of where this array of points is within the cubic samples.

Inclusions

Porosity

Fig. 12. Results of neutron computed tomography. Detected inclusions are shown for (a) Hex LP, (b) Hex HP, (c) Concentric samples. Detected pores are shown for (d) Hex LP, (e) Hex HP and (f) Concentric samples. Note that each panel shows two different views of the same data.

efficient (at a neutron wavelength of 1.5 Å) is 1.054 cm^{-1}. It is, therefore, likely that these inclusions are of the same chemistries as those observed on the fracture surface of the tensile test specimens (Fig. 7). Fig. 12(e) and (f) shows the presence of large open volumes within the sample.

4. Discussion

4.1. As-built and heat-treated microstructures

As both martensite and ferrite are BCC in 17-4 PH, changes in the XRD signal or EBSD Kikuchi pattern cannot be used to distinguish between them. Therefore, these phases must be identified by their morphology. As the BCC phase in the as-built microstructures shown in Fig. 2 exhibits a grain structure consistent with the solidification phase of LPBF material, it is surmised that this BCC phase is the solidification phase for 17-4 PH: δ-ferrite [14]. Therefore, the as-built microstructures consist of δ-ferrite and a small volume fraction of austenite. The high power fabrication condition results in a greater grain size along the build direction due to more pronounced epitaxial growth, as detailed in [14]. Both Table 3 and Fig. 2 show a large increase in austenite volume fraction following the CA heat treatment. Fig. 2 also shows the refinement of the now duplex martensitic-austenitic microstructure that this heat treatment induces. Based on the ICP-AES results displayed in Table 2 and Eqs. (1) and (2) [47], the Cr$_{eq}$/Ni$_{eq}$ ratios for the powder and the builds are calculated to be 1.99 and 2.19, respectively.

$$Cr_{eq}\ (wt\%) = Cr + 2(Si) + 1.5(Mo) + 5(V) + 5.5(Al) + 1.75(Nb) + 1.5(Ti) + 0.75(W) \tag{1}$$

$$Ni_{eq}\ (wt\%) = Ni + (Co) + 0.5(Mn) + 0.3(Cu) + 25(N) + 30(C) \tag{2}$$

The discrepancy between these two values is accounted for by the loss of more volatile elements during LPBF fabrication as well as the incorporation of impurities. The greater the Cr$_{eq}$/Ni$_{eq}$ ratio the greater the stability of ferrite/martensite. The lower this ratio, the greater the stability of austenite. A Cr$_{eq}$/Ni$_{eq}$ ratio greater than 1.5 will result in ferrite becoming the stable equilibrium solidification phase [24]. It is possible that the Cr$_{eq}$/Ni$_{eq}$ ratio for the powder used in this study (1.99) was not sufficiently high to obtain a fully martensitic microstructure after the CA heat treatment. Others in the field who reported a fully martensitic microstructure following this heat treatment listed powder compositions with greater Cr$_{eq}$/Ni$_{eq}$ ratios [17,18]. Further investigation on the effect of this ratio on phase transformation pathways in additively manufactured 17-4 PH will be the subject of further study.

4.2. Microstructure and mechanical property relationships

It can be seen in the tensile testing results presented in Table 4 and Fig. 5 that, in the as-built state, horizontally built Hex HP samples showed lower yield and ultimate tensile strengths than Hex LP or Raster samples. The greater laser power used in fabricating the Hex HP samples led to an increased average grain size in the as-built microstructures as shown in Fig. 2. Given that there is no major difference in the volume fractions of ferrite and austenite between these printing conditions (as shown in Table 3), the more refined microstructure will have an increased strengthening effect as per the Hall-Petch relationship [48]. Previous work by the current authors [49] has indicated that using the greater laser power during fabrication led to an increase in the clustering of Cu atoms in the as-built condition due to the effect of the intrinsic heat treatment of the laser powder bed fusion process. Given that the use of the lower laser power led to an increase in tensile strength, it can be surmised that the effect of the increase in Cu clustering is not the dominant factor in determining the strength of this material in the as-built state.

Dimpled fracture surfaces shown in Figs. 6–8 are the result of microvoid coalescence during ductile failure [50]. This demonstrates that all samples, in each heat-treated state, show ductile failure. Considering the prematurely failed as-built sample analysed in Fig. 9, the premature failure is likely due to the prevalence of lack of fusion porosity. This low ultimate tensile strength (669 MPa) means that the required plastic deformation accumulation to produce a strong ⟨110⟩ texture has not occurred. Comparing the ⟨001⟩ pole figures in Fig. 9, it can be seen that the as-built specimen which did not undergo premature failure still retains its cube texture resulting from solidification and epitaxial growth during fabrication, as outlined in Ref. [14]. This shows that the plastic deformation was accommodated by a rotation of the existing cube texture to align an average ⟨110⟩ texture with the build direction.

The difference in average KAM between the CA and CA-H900 samples in Fig. 10 is likely due to the fact that the CA-H900 sample analysed with EBSD experienced a much higher plastic strain before failure than the analysed CA sample. Correlating this with the average mechanical properties and their associated standard deviations, presented in Table 4, it can be surmised that this increased grain deformation at the fracture surface is not a consistent difference between samples in the CA and CA-H900 condition. However, increased KAM after H900 could be indicative of misorientation generated by precipitate formation. This is suggested to be the subject of further study.

There is no great difference between the values of impact toughness for the LPBF samples considered in this study for each printing condition. These as-built impact toughness values are inferior to wrought solution annealed (CA) 17-4 PH stainless steel but superior to wrought material in the CA-H900 condition [45].

Vertically built Hex HP samples were shown to have a greater ductility than either Hex LP or Raster samples. This is explained considering the morphology of their fracture surfaces presented in Fig. 8. The Hex LP sample shows a network of interconnecting lack of fusion defects indicated by red, dashed ellipses in Fig. 8(b), which were absent on the fracture surface of the Hex HP samples. The presence of these defects resulted in a reduced ductility in the Hex LP samples, as they enabled plastic instabilities to form at lower strain values. This shows that a greater laser power promoted greater remelting of previous layers, resulting in better interlayer fusion, reducing the prevalence of such defects [14]. This is consistent with the general finding in LPBF that a greater energy density results in an increased penetration depth (i.e., melt pool depth) which leads to a reduction in lack of fusion porosity [51]. The open columnar volumes present in the Hex HP build analysed in Fig. 12(e) align well with the build direction and are arranged at 60° to the sample axes (i.e., aligning with the scan direction), it can be surmised these are also lack of fusion pores resultant from an issue with the laser scan on a certain region of the powder bed. These are not thought to be reflective of a consistent difference between the Hex LP and Hex HP conditions.

It is expected from literature concerning 174 PH stainless steel [8,17,18] that heat treating to CA would result in an increase in yield stress due to the formation of a refined martensitic microstructure. However, the yield stress decreased after the CA heat treatment in all cases in this study. This is likely the result of the increase in the austenite volume fraction in the samples after heat treatment, as shown conclusively by the XRD results in Table 3. The characteristically high levels of work hardening after yielding are likely caused by the transformation of the austenite to martensite during mechanical testing, as is the case with transformation induced plasticity (TRIP) assisted steels [52]. The reduction in austenite volume fraction after mechanically testing the heat treated samples, shown by comparing Fig. 2 with Figs. 9 and 10, confirms that this phase transformation takes place during mechanical testing. Using digital image correlation, Shaffer et al.

[20] showed that the transformation of austenite to martensite in LPBF fabricated 17-4 PH results in Lüders banding across the gauge length during the yield plateau both in as-built and heat treated samples containing significant volume fractions of austenite. The authors also showed a second onset of Lüders banding in samples which showed a second discontinuity in the stress vs strain behaviour. Such tensile behaviour is also observed in Fig. 5 for the CA and CA-H900 samples considered in this study, as well as in 17-4 PH samples in literature containing substantial volume fractions of austenite [22]. This second stage of Lüders banding was shown to occur after most of the austenite within the microstructure had already transformed to martensite, without any resolvable change to the phase transformation behaviour with continued straining [20]. After the Lüders banding transformation region of the stress-strain curves, the significant hardening that follows is a result of continued transformation of the remaining austenite of this dual phase microstructure, with the transformation resulting in higher resistance against further deformation [20,52]. It has been reported for TRIP assisted steels that the ultimate failure of the part shortly follows the beginning of plastic deformation within the martensite, after the austenite has transformed to its fullest extent [53].

Ru et al. [54] performed in situ synchrotron X-ray diffraction during tensile tests on a Cu/ Steel nanolamellar composite. The Cu deformation was stated to be uniform. Similar secondary stress vs strain discontinuities were observed in some samples, as seen in this study and in literature. Both the initial discontinuity (yield plateau) and secondary discontinuity were shown by the XRD spectra to coincide with austenite to martensite transformations within the microstructure. TEM analysis showed that two morphologies of austenite were present within the microstructure: island-like and plate-like. It was proposed that the different morphologies of austenite on the observed length scale resulted in different mechanical stabilities. Therefore, it was surmised that island-like austenite transforms at the first discontinuity and the plate-like austenite transformed at the secondary discontinuity. This mechanism would comply with the relevant observations made in the current study and the studies in literature observing a secondary stress-strain discontinuity in TRIP-assisted steels [20,22]. Figs. 2 and 3 show that the austenite present after the CA heat treatment in the samples considered in the current work varies in scale from 10 s of micrometres to 100 s of nanometres. To confirm that Ru et al.'s [54] proposed mechanism is taking place would require high-resolution in-situ microscopy or microstructural analysis of interrupted mechanical tests to determine which populations of austenite transform at each point in the tensile test. This should be the subject of future study.

Fig. 4(c) and (d) shows that the Cu distribution on the atomic scale is random in both the CA and CA-H900 samples. This means that, for both conditions, the position of the Cu atoms is random relative to one another meaning that Cu atoms have not yet begun to form clusters and/or precipitates within the matrix. This is expected in the CA condition, as Cu dissolves in austenite at high temperature before quenching gives sufficiently fast cooling to inhibit diffusion. The H900 ageing treatment is expected to result in the formation of such clusters/precipitates in 17-4 PH as are observed following conventional processing routes [55,56], but Fig. 4(d) shows that this does not occur. Previous work has shown that Cu clustering does occur in both the low power and high power conditions in the as-built state under the effect of the intrinsic heat treatment during the LPBF process [49]. The fact that ageing to the H900 condition did not result in any significant increase in strength is undesirable and contrasts with some previous studies [8,17,18]. The absence of Cu precipitation in the APT data for the CA-H900 sample is consistent with observations in literature that the presence of austenite within the microstructure of 17-4 PH before ageing will reduce the capacity for age hardening

[10,17,57]. As Cu is more soluble in austenite than in either ferrite or martensite [5,17,58], during ageing it could be more energetically favourable for Cu to stay in solid solution in the austenite rather than forming precipitates [17,57].

Fig. 5(c) and (d) shows that, after the CA heat treatment, samples which were fabricated with a higher laser power (stress-strain curves shown in red) exhibited a shorter yield plateau before the onset of work hardening. This is a consistent difference observed between all samples tested in this study, not only in the representative curves shown in Fig. 5. Table 3 and Fig. 2 do not show any discernible shift in phase fraction to cause this change in tensile behaviour. However, the average BCC grain size is significantly higher in the Hex HP-CA sample than in the Hex LP-CA sample (having average area weighted grain diameters of 2.5 μm and 1.3 μm, respectively), which may have led to this change in work hardening behaviour.

At higher magnification, the decohesion of martensitic packet boundaries beneath the fracture surface is evident in the CA sample (Fig. 10(e–h)). This indicates intergranular failure resulting from a comparative weakness of the packet boundaries to the packet interiors. However, the micrographs of the corresponding fracture surface, shown in Fig. 6(g–i), show a dimpled surface indicative of ductile failure via microvoid coalescence. Despite delamination occurring at packet boundaries adjacent to the fracture surface, this failure remains ductile and not brittle, explaining the absence of a faceted fracture surface typical of intergranular failure [50]. This type of intergranular delamination continuing into the subsurface of the crack region is not observed across all samples that underwent heat treatment. It is speculated that the absence of these signs of failure allowed the CA-H900 samples analysed in Fig. 10 to accumulate greater plastic deformation up to failure, as shown by the KAM map in Fig. 10(l).

4.3. Residual stress analysis

The presence of a tensile residual stress at the surface of as-built metal AM parts and a compressive stress in the interior (as shown in Fig. 11) is well established [25,26,33]. Using a layer-by-layer model (excluding the effect of individual tracks), this arises as a newly deposited layer contracts when it cools on top of the cooler previous layer. The previously solidified layers and the substrate resist the contraction of the new layer resulting in a tensile residual stress within the plane of the build layers throughout the build, with this stress increasing with build height [25,59]. After removal from the build plate, residual stresses in the part and build plate can no longer interact with one another, meaning partial stress relaxation occurs through the part. This results in the observed residual stress profile in these samples; tensile along the top and bottom surfaces, compressive in the interior [25]. As the scanning direction of the hexagonal bidirectional laser raster in samples Hex LP and Hex HP in Fig. 11 was rotated 90° in each scan layer, the results presented in Fig. 11 are assumed to have 90° rotational symmetry.

Comparing the residual stress distributions shown for the cubic Hex LP and Hex HP builds in Fig. 11, the profiles of residual stress through these builds are almost exact matches, likely due to the fact that the scanning pattern and scan rotation remains constant between these two samples. Additionally, a slight decrease in the residual stress magnitude can be observed along z and x with increasing laser power. It is expected that this is the result of a greater laser power causing a larger melt pool which leads to a reduction in cooling rate and therefore a more uniform contraction of the material [59]. Both samples show a similar biaxial residual stress state (in tension in x and y) on the top and bottom surface of the build. Midway along the build height, on the sides of the build, the residual stress is almost uniaxial with σ_{zz} ~300 MPa and σ_{yy}

~0 MPa. Given that there is no great difference between residual stress magnitude and distribution with changing laser power for this scanning strategy, it can be surmised that residual stress had a minimal effect on observed differences in mechanical properties between the Hex LP and Hex HP fabrication condition.

There is a great difference in both the magnitude and 3D profiles of residual stresses within the cubic builds fabricated with a hexagonal scanning strategy and fabricated with a concentric scanning strategy (see Fig. 11). This shows the significant dependence of residual stress within as-built LPBF builds on the scanning strategy used. The concentric scanning pattern has allowed more residual stress to accumulate across layers, which has previously been observed in some samples printed with long scanning paths without rotation [32,60]. This does not apply to the hexagonal scanning strategy due to the 90° laser raster scan rotation between layers [32] or in scenarios where scanning paths become so short that the effective melt pool shape and subsequent local thermal history are affected [61]. Beyond the absence of laser scan rotation between build layers, an effect of the concentric scanning strategy is that as the laser scans concentrically inwards in each layer, material closer to the centre of the scan has less time to solidify and cool before the next adjacent pass of the laser. This effect has previously been observed to affect the local phase fraction within LPBF builds in this alloy [14]. It also results in a gradient of cooling rates as well as thermal contraction behaviour through the build. This means that regions at the centre of the concentric build retain heat for longer as regions further away from the centre in the same layer will cool faster. Consequently, material at the centre will yield at a lower yield stress due to the greater temperature, then cool and contract. This contraction is then resisted by the material adjacent to the centre, putting these areas into tension. This results in the column of high compressive stress in this cube, coinciding with the centre of the scanning pattern in each layer. Kudzal et al. [16] attributed inferior mechanical properties in their 17-4 PH LPBF builds fabricated using a concentric scanning pattern to the alignment of inter melt track defects creating low energy crack paths during loading. Whilst this effect may also play a role, the mechanical properties will have also been negatively impacted by the high residual stresses incurred by this scanning strategy. Pant et al. [37] showed a slight reduction in residual stress in a sample produced with a concentric scanning strategy, however this scanning strategy was elongated meaning that inward progress of the laser path did not align to a point but rather a line scan. The resulting scan path is therefore incomparable in terms of residual stress to the concentric scanning strategy considered in the present work.

In the Concentric sample, the strongest tensile residual stresses are observed along the y direction (Fig. 11). Given the plane in which measurements were taken, this corresponds to tensile stresses along the scanning direction, which does not change between layers. The presence of high tensile residual stresses in regions away from the core of this build, potentially exceeding the local ultimate tensile strength, likely played a role in the presence of the internal crack shown in Fig. 12(f). Given this crack's geometry around the pattern of residual stress in the build (Fig. 11), the strain incurred by its formation will have allowed local stress relaxation [25].

As seen in Table 5, the measured maximum tensile residual stresses observed in the Concentric sample are much lower in magnitude compared to the compressive stress in this sample. This is due to the fact that this high compressive stress occurs in a relatively small columnar volume in the centre of the Concentric sample, whereas more moderate tensile stresses are distributed over a larger volume. Furthermore, the maximum tensile residual stresses in as-built LPBF parts will occur at the free surfaces of the build [25,26] so it follows that the maximum tensile stresses in these samples did not occur at the measured sites, but extrapolating the

trends in residual stresses allows the visualisation of these maximum tensile stresses at the surface. If the parts had warped after fabrication, it could be easily surmised that the maximum tensile stress, occurring at the free surface, is equal to the yield stress of the as-built material [25] (750–900 MPa, as shown by the tensile testing data in Table 4). However, no warping of the parts was observed in this study, so the maximum tensile residual stresses at the surface must be lower than the yield stress in all cases.

5. Conclusions

The microstructure and mechanical properties of LPBF fabricated 17-4 PH stainless steel have been investigated systematically both before and following heat treatments. The as-built resultant residual stress distributions from different printing strategies have been measured using neutron diffraction and quantified. The key findings from this study are as follows:

(1) The increase in laser power from 127.5 to 161.5 W led to a ~6 % decrease in the yield strength of the as-built LPBF fabricated 17-4 PH stainless steel samples when loaded normal to the build direction. When tested along the build direction, a greater laser power promoted better interlayer cohesion resulting in a ductility increase by a factor of ~3.3.

(2) Solution annealing and quenching results in austenite formation in the matrix of the samples investigated in this study, presumably due to the low Cr_{eq}/Ni_{eq} ratio.

(3) The presence of a large volume fraction of austenite in the heat-treated samples had the effect of reducing the yield stress but increasing the work hardening capacity of the builds due to the transformation of austenite to martensite by the TRIP effect.

(4) The absence of any Cu clustering or precipitation behaviour was observed in the heat-treated samples resulting from the high volume fraction of austenite within the microstructure.

(5) Scanning strategy was observed to have a more significant effect on the 3D residual stress distribution within the builds than laser power. Our study reveals that large concentric scans are to be avoided in order to minimise the build-up of residual stress.

(6) This work has demonstrated the interconnected impact of scanning strategy, laser power, and heat treatments on the microstructure and mechanical properties, and in turn the suitability of LPBF 17-4 PH parts for engineering applications. This coupling of the properties and the fabrication process drives towards the AM production of materials with optimised properties.

Declaration of competing interest

The authors declare that they have no known competing financial interests or personal relationships that could have appeared to influence the work reported in this paper.

Acknowledgments

Supplementary materials

Supplementary material associated with this article can be found, in the online version, at doi:10.1016/j.jmst.2024.01.080.

References

[1] T. DebRoy, H.L. Wei, J.S. Zuback, T. Mukherjee, J.W. Elmer, J.O. Milewski, A.M. Beese, A. Wilson-Heid, A. De, W. Zhang, Prog. Mater. Sci. 92 (2018) 112–224.
[2] S. Yang, Y.F. Zhao, Int. J. Adv. Manuf. Technol. 80 (2015) 327–342.
[3] Findings from Wohlers Report 2022: Taking a Chance on New Technologies and the Evolving Materials Mix, Metal AM, 2022.
[4] U.K. Viswanathan, S. Banerjee, R. Krishnan, Mater. Sci. Eng. 104 (1988) 181–189.
[5] C.N. Hsiao, C.S. Chiou, J.R. Yang, Mater. Chem. Phys. 74 (2002) 134–142.
[6] ASM International Handbook Committee, in: ASM Handbook, 4, Heat Treating, ASM International, 1991, pp. 769–792.
[7] J.H. Wu, C.K. Lin, Metall. Mater. Trans. A 33 (2002) 1715–1724.
[8] N. Haghdadi, M. Laleh, M. Moyle, S. Primig, J. Mater. Sci. 56 (2020) 64–107.
[9] L.E. Murr, E. Martinez, J. Hernandez, S. Collins, K.N. Amato, S.M. Gaytan, P.W. Shindo, J. Mater. Res. Technol. 1 (2012) 167–177.
[10] T.-H. Hsu, Y.-J. Chang, C.-Y. Huang, H.-W. Yen, C.-P. Chen, K.-K. Jen, A.-C. Yeh, J. Alloy. Compd. 803 (2019) 30–41.
[11] S. Vunnam, A. Saboo, C. Sudbrack, T.L. Starr, Addit. Manuf. 30 (2019) 100876.
[12] B.L. Facchini, V. Jr, I. Lonardelli, E. Magalini, P. Robotti, A. Molinari, Adv. Eng. Mater. (2010) 184–188.
[13] M. Alnajjar, F. Christien, K. Wolski, C. Bosch, Addit. Manuf. 25 (2019) 187–195.
[14] M.S. Moyle, N. Haghdadi, X.Z. Liao, S.P. Ringer, S. Primig, J. Mater. Sci. Technol. 117 (2022) 183–195.
[15] Y. Sun, R.J. Hebert, M. Aindow, Mater. Des. 156 (2018) 429–440.
[16] A. Kudzal, B. McWilliams, C. Hofmeister, F. Kellogg, J. Yu, J. Taggart-Scarff, J. Liang, Mater. Des. 133 (2017) 205–215.
[17] T. LeBrun, T. Nakamoto, K. Horikawa, H. Kobayashi, Mater. Des. 81 (2015) 44–53.
[18] P.D. Nezhadfar, R. Shrestha, N. Phan, N. Shamsaei, Int. J. Fatigue 124 (2019) 188–204.
[19] E.A. Lass, M.R. Stoudt, M.E. Williams, Metall. Mater. Trans. A 50 (2019) 1619–1624.
[20] D.J. Shaffer, A.E. Wilson-Heid, J.S. Keist, A.M. Beese, T.A. Palmer, Mater. Sci. Eng. A 817 (2021) 141363.
[21] S.D. Meredith, J.S. Zuback, J.S. Keist, T.A. Palmer, Mater. Sci. Eng. A 738 (2018) 44–56.
[22] H.K. Rafi, D. Pal, N. Patil, T.L. Starr, B.E. Stucker, J. Mater. Eng. Perform. 23 (2014) 4421–4428.
[23] S. Cheruvathur, E.A. Lass, C.E. Campbell, JOM 68 (2016) 930–942.
[24] S. Sabooni, A. Chabok, S.C. Feng, H. Blaauw, T.C. Pijper, H.J. Yang, Y.T. Pei, Addit. Manuf. 46 (2021) 102176.
[25] P. Mercelis, J.P. Kruth, Rapid Prototyp. J. 12 (2006) 254–265.
[26] C. Li, Z.Y. Liu, X.Y. Fang, Y.B. Guo, Proc. CIRP 71 (2018) 348–353.
[27] P.J. Withers, H.K.D.H. Bhadeshia, Mater. Sci. Technol. 17 (2001) 355–365.
[28] T. Mukherjee, W. Zhang, T. DebRoy, Comput. Mater. Sci. 126 (2017) 360–372.
[29] Y. Lu, S. Wu, Y. Gan, T. Huang, C. Yang, L. Junjie, J. Lin, Opt. Laser Technol. 75 (2015) 197–206.
[30] Z.C. Fang, Z.L. Wu, C.G. Huang, C.W. Wu, Opt. Laser Technol. 129 (2020) 106283.
[31] W. Chen, T. Voisin, Y. Zhang, J.B. Florien, C.M. Spadaccini, D.L. McDowell, T. Zhu, Y.M. Wang, Nat. Commun. 10 (2019) 4338.
[32] J. Robinson, I. Ashton, P. Fox, E. Jones, C. Sutcliffe, Addit. Manuf. 23 (2018) 13–24.
[33] A.S. Wu, D.W. Brown, M. Kumar, G.F. Gallegos, W.E. King, Metall. Mater. Trans. A 45 (2014) 6260–6270.
[34] M. Masoomi, N. Shamsaei, R.A. Winholtz, J.L. Milner, T. Gnäupel-Herold, A. Elwany, M. Mahmoudi, S.M. Thompson, Data Brief 13 (2017) 408–414.
[35] N. Nadammal, S. Cabeza, T. Mishurova, T. Thiede, A. Kromm, C. Seyfert, L. Farahbod, C. Haberland, J.A. Schneider, P.D. Portella, G. Bruno, Mater. Des. 134 (2017) 139–150.
[36] K. An, L. Yuan, L. Dial, I. Spinelli, A.D. Stoica, Y. Gao, Mater. Des. 135 (2017) 122–132.
[37] P. Pant, F. Salvemini, S. Proper, V. Luzin, K. Simonsson, S. Sjöström, S. Hosseini, R.L. Peng, J. Moverare, Mater. Des. 214 (2022) 110386.
[38] H.R. Lashgari, C. Kong, E. Adabifiroozjaei, S. Li, Wear 457 (2020) 203367.
[39] P.W. Trimby, J.M. Cairney, Adv. Mater. Proc. 172 (2014) 13–16.
[40] D.B. Williams, C.B. Carter, Transmission Electron Microscopy: A Textbook For Materials Science, 3rd ed., Springer, 1996.
[41] O. Kirstein, V. Luzin, U. Garbe, Neutron News 20 (2009) 34–36.
[42] R.A. Winholtz, in: Measurement of Residual and Applied Stress Using Neutron Diffraction, Springer, 1992, pp. 131–145.
[43] U. Garbe, T. Randall, C. Hughes, G. Davidson, S. Pangelis, S.J. Kennedy, Phys. Proc. 69 (2015) 27–32.
[44] D. Micieli, T. Minniti, G. Gorini, SoftwareX 9 (2019) 260–264.
[45] H.J. Rack, D. Kalish, Metall. Mater. Trans. B 5 (1974) 1595–1605.
[46] S. Suwas, R.K. Ray, Crystallographic Texture of Materials, first ed., Springer, 2014.
[47] M. Shirdel, H. Mirzadeh, M.H. Parsa, Mater. Charact. 103 (2015) 150–161.

[48] M.F. Ashby, D.R.H. Jones, Engineering Materials 1: An Introduction to Properties, Applications, and Design, 4th ed., Butterworth-Heinemann, 2012.

[49] M.S. Moyle, N. Haghdadi, W.J. Davids, X.Z. Liao, S.P. Ringer, S. Primig, Scr. Mater. 219 (2022) 114896.

[50] T.L. Anderson, Fracture Mechanics: Fundamentals and Applications, third ed., Taylor & Francis, 2005.

[51] T. Mukherjee, J.S. Zuback, A. De, T. DebRoy, Sci. Rep. 6 (2016) 19717.

[52] H. Bhadeshia, R. Honeycombe, Steels: Microstructure and Properties, fourth ed., Butterworth-Heinemann, 2017.

[53] B.L. Ennis, E. Jimenez-Melero, E.H. Atzema, M. Krugla, M.A. Azeem, D. Rowley, D. Daisenberger, D.N. Hanlon, P.D. Lee, Int. J. Plast. 88 (2017) 126–139.

[54] Y. Ru, K.Y. Yu, F. Guo, Y. Ren, L. Cui, Mater. Sci. Eng. A 734 (2018) 77–84.

[55] Z. Wang, H. Li, Q. Shen, W. Liu, Z. Wang, Acta Mater. 156 (2018) 158–171.

[56] G. Yeli, M.A. Auger, K. Wilford, G.D.W. Smith, P.A.J. Bagot, M.P. Moody, Acta Mater. 125 (2017) 38–49.

[57] M. Murayama, Y. Katayama, K. Hono, Metall. Mater. Trans. A 30 (1999) 345–353.

[58] G. Salje, M. Feller-Kniepmeier, J. Appl. Phys. 48 (1977) 1833–1839.

[59] N.C. Levkulich, S.L. Semiatin, J.E. Gockel, J.R. Middendorf, A.T. DeWald, N.W. Klingbeil, Addit. Manuf. 28 (2019) 475–484.

[60] J.P. Kruth, J. Deckers, E. Yasa, R. Wauthlé, J. Eng. Manuf. 226 (2012) 980–991.

[61] M. Haines, F. List, K. Carver, D. Leonard, A. Plotkowski, C. Fancher, R. Dehoff, S. Babu, Addit. Manuf. 50 (2022) 102578.